mater.scichina.com link.springer.com

Published online 12 June 2020 | https://doi.org/10.1007/s40843-020-1333-9
Sci China Mater 2020, 63(10): 2050–2061

Highly efficient and broad electromagnetic wave absorbers tuned *via* topology-controllable metal-organic frameworks

Peng Miao, Jianxin Chen, Yusheng Tang, Kai-Jie Chen and Jie Kong*

ABSTRACT **Advanced electromagnetic (EM) wave absorbing materials with strong absorption and broad bandwidth are important for military stealth and elimination of microwave pollution in consumers' electronics. Metal organic framework (MOF)-derived metal/carbon hybrids with ordered structure are significantly urgent in this field. In this contribution, we presented a design strategy of hollow cage-like or solid box-like magnetic/dielectric Fe/Co/C and dielectric Fe/Mn/C EM wave absorbing nanomaterials *via* pyrolyzing Prussian blue's analogs with controllable topology and phase composition. The solid box-like Fe/Co/C and hollow cage-like Fe/Mn/C showed favorable absorption property with a broad effective absorption bandwidth (EAB) and a low reflection loss (RL). Especially, the EAB of 8.8 GHz at a thickness of 2.5 mm for solid box-like Fe/Co/C nanocomplex prepared at 900°C is a new record for this type of materials. The design and tuning strategy for EM wave absorbers derived from topology-controllable MOF is important for EM functional materials possessing great potential in military stealth and consumers' electronics.**

Keywords: electromagnetic wave absorber, MOF, Prussian blue's analogs, topology, pyrolysis

INTRODUCTION

Advanced electromagnetic (EM) wave absorbing materials with strong absorption, broad bandwidth, thin thickness and low density have received numerous attentions due to urgent demand in military stealth and elimination of microwave pollution or radiation in consumers' electronics and base stations of wireless networks [1–3]. Various magnetic materials, such as ferrites, Fe-, Co-, Ni-based nanoparticles and alloys, as well as carbon family materials including carbon fibers, carbon nanotubes and graphenes were mainly utilized to match the engineering applications of EM wave absorbing materials in form of coating, sealing or composites [4,5].

Metal-organic frameworks (MOFs) integrated the features of organic-inorganic hybrids, high porosity, ultrahigh specific surface area and tunable topological structure [6,7]. Their diversity of compositions and topological structures give favorable functionalities with great potential in gas separation/storage, catalysis and biomedicine [8–11], etc. In our previous work [6], a synergistic sorbent separation method was presented for the one-step production of polymer-grade C_2H_4 from ternary ($C_2H_2/C_2H_6/C_2H_4$) or quaternary ($CO_2/C_2H_2/C_2H_6/C_2H_4$) gas mixtures by using MOFs. Especially, MOF-derived metal/carbon composites after pyrolysis have drawn significant attention in various fields [12–14]. They might possess desirable EM wave absorbing or shielding ability. As expected, the derived Co/C composite with well-dispersed magnetic cobalt nanoparticles inherited the topological structure of ZIF-67 crystals, showing effective absorption even at high temperature, i.e., a minimum reflection loss (RL_{min}) of −35.3 dB and an effective absorption bandwidth (EAB) of 5.8 GHz measured at 500°C [15]. The modified ZIF-67-derived hybrids with SiC [16], ZIF-8 [17,18], MXene [19], poly(dimethylsilylene)diacetylene (PDSDA) [20], carbon nanotubes (CNTs) [21], multiwalled CNTs (MWCNTs) [22,23], V_2O_3 [24], Co_9S_8 [25], etc., were extensively studied. Meanwhile, other MOFs including two-dimensional (2D) Co-MOF [26], Co-MOF-74 [27], MIL-88A(Fe) [28], MIL-101(Fe) [29], CPT-1-Co [30], and Fe^{III}-MOF-5 [31] with controllable topologies also received attentions in the fields of EM functional materials.

Prussian blue (PB) and its analogs (PBAs) are a class of

MOE Key Laboratory of Materials Physics and Chemistry in Extraordinary Conditions, Shaanxi Key Laboratory of Macromolecular Science and Technology, School of Chemistry and Chemical Engineering, Northwestern Polytechnical University, Xi'an 710072, China
* Corresponding author (email: kongjie@nwpu.edu.cn)

MOFs with cubic structure as well as a general chemical formula of $A_2M[M'(CN)_6]$ (A = alkaline metal ions, zeolitic water, M/M′ = transition metals) [32,33]. The octahedral $[M(CN)_6]^{n-}$ complex is coordinating M^{n+} with nitrogen bonding. Their crystal structures were verified by Keggin and Miles [34]. Based on PBAs, a series of complexes were synthesized with hollow, core shell or solid topologies showing potentials in electrocatalysts [35], energy storage [36], electrocatalytic water splitting [37], and EM wave absorbing materials [38]. For example, the Fe/C nanocubes derived from PB show a RL_{min} of −22.6 dB at 15 GHz and an EAB of 5.3 GHz (12.7–18 GHz) with a thickness of 2 mm [39]. The Fe/Co/C complex can also be obtained through the pyrolysis of PBAs, whose absorption is superior to that of single metallic complex [40].

As well-known, besides the suitable EM parameters to ensure impedance matching and energy attenuation [41], the topological structure of MOF derivates can also direct EM wave toward multi scattering and polarization loss [38,42]. These factors can be combined to enhance microwave attenuation and broaden EAB. Actually, some complicated factors, such as phase composition, morphology and temperature, affect microwave attenuation [43]. But the previous design mainly focused on the EM parameters of a specific absorber in a given condition of morphology or phase composition. However, the comprehensive effects of topology and phase composition were seldom considered. So EM wave absorption efficiency, either EAB or RL, was not favorable as expected.

In this contribution, we presented a design strategy of hollow cage-like or solid box-like magnetic/dielectric Fe/Co/C and dielectric Fe/Mn/C EM wave absorbing nanocomplexes *via* pyrolyzing PBAs with controllable topology and phase composition. The hollow cage- or solid box-like Fe/Co/C and hollow Fe/Mn/C nanocomplexes show a broad and favorable absorbing ability from the viewpoint of either EAB or RL. Especially, the EAB of 8.8 GHz at a thickness of 2.5 mm for solid box-like Fe/Co/C nanocomplex prepared at 900°C is a new record for this type of materials. It is definitely important for the design of highly efficient EM wave absorbing materials in a comprehensive perspective, which possess great potential in antenna housings, areo-engines and stealth aircrafts.

EXPERIMENTAL SECTION

Synthesis of hollow Fe-Co PBA cages

The hollow Fe-Co PBA cages were synthesized by chemical co-precipitation as reported previously [44]. Briefly, a solution A was formed by dissolving 0.2 g of potassium hexacyanoferrate (III) in 60 mL of deionized water. Cobalt (II) acetate tetrahydrate (0.3 g), trisodium citrate dihydrate (0.3 g) and polyvinyl pyrrolidone (PVP, 3.0 g, K30, M_w = 40,000 Da) were dissolved in 40 mL of deionized water to form a solution B. Solution B was slowly added to solution A within 1 min under magnetic stirring. After being stirred continuously for 1 min, the mixed solution was transferred to an oven and reacted at 80°C for 24 h. The purple-black precipitation was washed with deionized water and ethanol for three times, and dried overnight at 70°C.

Synthesis of hollow Fe-Mn PBA cages

Similarly, the hollow Mn-Fe PBA cages were obtained through a method modified from Ref. [45]. Typically, 16.4 mg of $K_3[Fe(CN)_6]$ was dissolved in a C_2H_5OH/H_2O (5/5 mL) system under agitated stirring to give a transparent solution C. Solution D was prepared by dissolving 25.4 mg $MnSO_4{\cdot}H_2O$, 15.0 mg trisodium citrate dihydrate and 0.3 g PVP (K-30) in a C_2H_5OH/H_2O (5/5 mL) system under stirring for 30 min. Solution C was added to solution D slowly with a syringe (20 mL). After being stirred for 10 min at room temperature, the mixed solution aged for 24 h without interruption. The white precipitate was collected by filtration and washed with ethanol for three times, and the hollow Fe-Mn PBA cages were obtained by drying the sample in an oven at 70°C.

Synthesis of solid Fe-Co PBA box

The solid Fe-Co PBA boxes were synthesized by the chemical co-precipitation method as reported previously [46], which is similar to the synthesis of hollow Fe-Co PBA cages, except for the addition of trisodium citrate dihydrate and PVP in the solution B.

Synthesis of solid Fe-Mn PBA box

The solid Mn-Fe PBA boxes were synthesized by the co-precipitation method [45], similar to the synthesis of hollow Fe-Mn PBA cages, except for the addition of trisodium citrate dihydrate in the solution D. The resultant white precipitates were collected by centrifugation, washed with ethanol for several times, and finally dried in an oven at 70°C overnight.

Preparation of Fe/Co/C and Fe/Mn/C nanocomplexes

The as-synthesized hollow Fe-Co or Fe-Mn PBA cages and solid Fe-Co or Fe-Mn PBA boxes were pyrolyzed in a tube-furnace (GSL-1700X, Kejing New Mater. Ltd., Hefei,

China) at 800 and 900°C, respectively, for 2 h with a heating rate of 0.5 K min^{-1} in argon. The nanocomplexes were named as hollow Fe/Co/C-800, hollow Fe/Co/C-900, solid Fe/Co/C-800, solid Fe/Co/C-900, hollow Fe/Mn/C-800, hollow Fe/Mn/C-900, solid Fe/Mn/C-800 and solid Fe/Mn/C-900 according to topological structures and pyrolyzed temperatures, respectively.

Characterizations

X-ray diffraction (XRD) patterns of the samples were collected on a Shimadzu 7000 XRD using Cu Kα radiation (λ = 0.15406 nm) with a scanning voltage of 30 kV, and a scanning current of 30 mA. The morphology and structure were scanned using a field emission scanning electron microscope (FESEM) (FEI, Verios G4) and transmission electron microscope (TEM) (FEI, Talos F200X) equipped with energy dispersive spectroscopy (EDS). Element composition was analyzed by X-ray photoelectron spectroscopy (XPS) on a Kratos Axis Ultra DLD using Al Kα radiation ($h\nu$ = 1486.6 eV) with a scanning voltage of 15 kV, and a scanning current of 10 mA. The magnetic performance was surveyed by hysteresis loop using vibrating sample magnetometers (Lake Shore VSM 7307). The Brunauer-Emmet-Teller (BET) specific surface area and pore size distribution were measured by high-performance multi-channel fully automatic surface and pore analyzer (BeiSbiDe3H-2000PS2, China) using N_2 at 77 K. Thermogravimetric analysis (TGA) (NETZSCH STA449, Germany) was carried out under a flow of argon with a temperature ramp of 10°C min^{-1} from room temperature to 1000°C.

EM wave absorption measurement

The EM parameters of the nanocomplexes were measured by a vector network analyzer (VNA, Anritsu, MS46322B) using the transmission/reflection coaxial method. The composite (absorbers/paraffin = 1:2, wt.%) was pressed into a coaxial ring with an outer diameter (ϕ_o) of 7.00 mm and an inner diameter (ϕ_i) of 3.04 mm in the frequency range of 2–18 GHz.

RESULTS AND DISCUSSION

PBAs and derived Fe/Co/C and Fe/Mn/C nanocomplexes with controllable topology

The synthetic routes of PBAs and their pyrolyzed nanocomplexes are schematically illustrated in Fig. 1. The hollow cages and solid boxes of Fe-Co PBAs or Fe-Mn PBAs were synthesized through coprecipitation methods, where the ion exchange reaction of bivalent Co^{2+} or Mn^{2+} ions and cyanide ferrate occurred in deionized water or ethanol/deionized water solution. The as-synthesized hollow Fe-Co PBA cages (Fig. 2a), hollow Fe-Mn PBA cages (Fig. 3a) and solid Fe-Co PBA boxes (Fig. 2d), solid Fe-Mn PBA boxes (Fig. 3d) were observed in TEM images. Either hollow cages or solid boxes show a well-defined hexahedron shape with a size in the range of 200–500 nm. Meanwhile, the EDS elemental mapping images

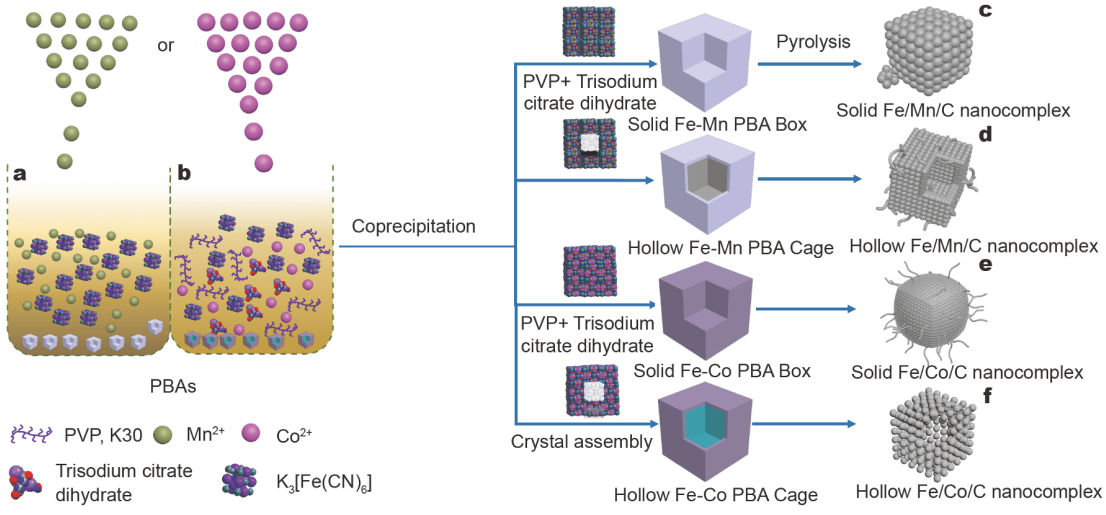

Figure 1 Schematic illustration of the fabrication route toward hollow PBA cages and solid PBA boxes and their derived nanocomplexes. (a) Synthesis of solid Fe-Co and Fe-Mn PBAs without PVP and trisodium citrate dihydrate. (b) Synthesis of hollow Fe-Co and Fe-Mn PBAs with PVP and trisodium citrate dihydrate. Preparation route of solid Fe/Mn/C (c), hollow Fe/Mn/C (d), solid Fe/Co/C (e) and hollow Fe/Co/C nanocomplexes (f), respectively.

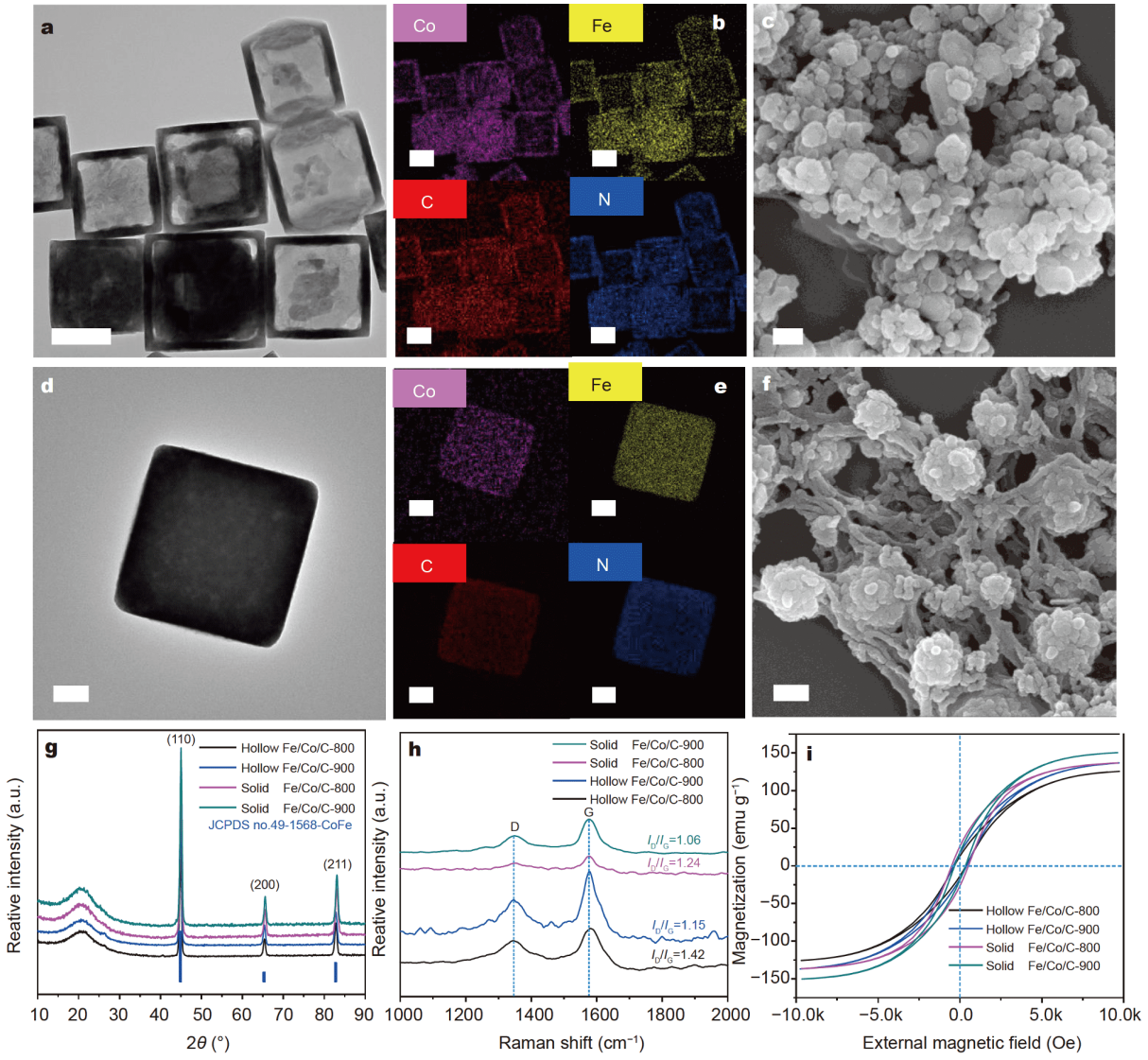

Figure 2 The topologies and phase compositions of hollow cages and solid boxes of Fe-Co PBAs and their pyrolyzed Fe/Co/C nanocomplexes. (a) TEM image and (b) corresponding element mapping (Fe, Co, C, and N) of Fe-Co PBA hollow cages. (c) SEM image of hollow Fe/Co/C-800. (d) TEM image and (e) corresponding element mapping (Fe, Co, C, and N) of Fe-Co PBA solid boxes. (f) SEM image of solid Fe/Co/C-800. (g) PXRD patterns, (h) Raman spectra and (i) hysteresis loops of pyrolyzed Fe/Co/C nanocomplexes measured at room temperature. Scale bar: 200 nm.

in Figs 2b, e and 3b, e clearly confirm the uniform distribution of Fe/Co or Fe/Mn elements in either hollow cage or solid box. The powder XRD (PXRD) patterns of hollow and solid PBAs in Fig. S1 (Supplementary information) well matched the peaks of potassium ferricyanide frameworks. The phase purity of the cubic PBAs verified their high crystallinity as supposed. The different topological structures can be obtained by controlling the usage or absence of PVP and trisodium citrate dihydrate. PVP was the key factor for forming uniform solid cubic PBAs without trisodium citrate dihydrate. The amide group of PVP would weakly coordinate with Co^{2+} or Mn^{2+} ions during the nucleation and growth of hollow Fe-Co and Fe-Mn PBAs. Therefore, the hollow structures of PBAs can be synthesized during the etching of trisodium citrate dihydrate [44,47].

To investigate their thermal behaviors, TGA was carried out under argon atmosphere in a temperature range of 40–1000°C. As shown in Fig. S2, the PBAs with different topologies showed similar thermolysis profiles. The initial weight loss of solid and hollow samples up to ~155 and ~180°C can be mainly attributed to the evaporation

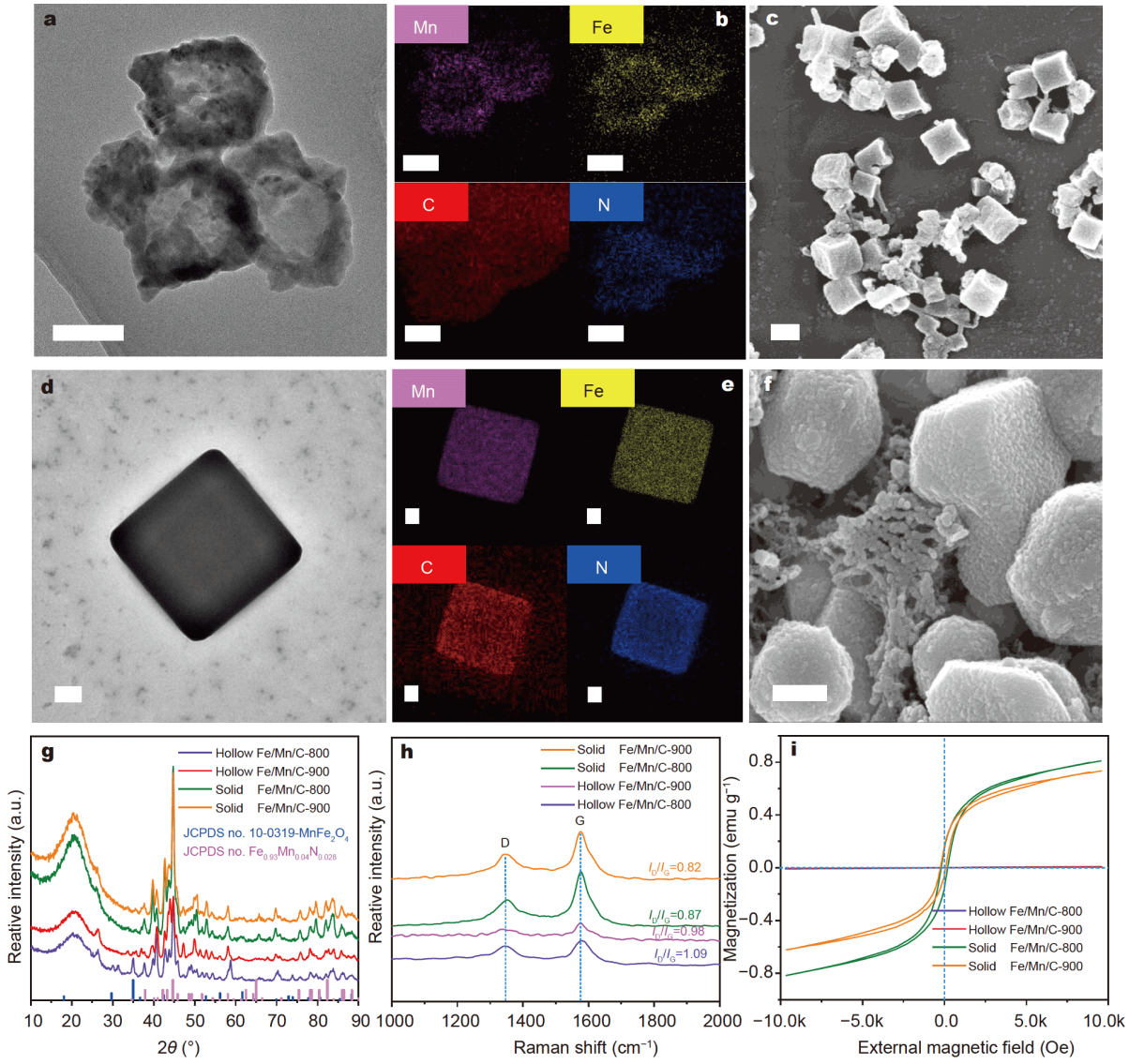

Figure 3 The topologies and phase compositions of hollow cages and solid boxes of Fe-Mn PBAs and their pyrolyzed Fe/Mn/C nanocomplexes. (a) TEM image and (b) corresponding element mapping (Fe, Mn, C, and N) of Fe-Mn PBA hollow cages. (c) SEM image of hollow Fe/Mn/C-800. (d) TEM image and (e) corresponding element mapping (Fe, Mn, C, and N) of Fe-Mn PBA solid boxes. (f) SEM image of solid Fe/Mn/C-800. (g) PXRD patterns, (h) Raman spectra and (i) hysteresis loops of pyrolyzed Fe/Mn/C nanocomplexes measured at room temperature. Scale bar: 200 nm.

of water in PBAs. As the temperature rose, the decomposition and weight loss of solid and hollow PBAs occurred above 550°C. To ensure the ideal preparation of EM wave absorbing nanocomplex, the pyrolysis temperature of 800–900°C might be a good choice. After pyrolysis of PBAs, the obtained Fe/Co/C and Fe/Mn/C nanocomplexes were partially collapsed and nearly remained the hollow cage-like or solid box-like shapes as depicted in Fig. 1c–f. For solid Fe/Co/C (Fig. 2f) and Fe/Mn/C (Fig. 3f) nanocomplexes, some nanoparticles gradually dissociated from the box surfaces, where the carbon nanorods were generated *via* transition metal catalysis. The solid Fe/Co/C nanocomplex was wrapped with more nanorods than the solid Fe/Mn/C nanocomplex under the same pyrolysis temperature. Obviously, for the hollow Fe/Co/C nanocomplex (Fig. 2c), some nanoparticles were filled on or between cubic cages. On the contrary, the hollow cages of Fe/Mn/C nanocomplex

(Fig. 3c) were identical only with a few collapsed particles.

PXRD was utilized to confirm their phase compositions and crystalline features. As shown in Fig. 2g, the diffraction peaks of hollow and solid Fe/Co/C nanocomplexes at 44.9°, 65.3° and 82.7° can be assigned to the (100), (200) and (211) planes of cubic CoFe crystal (JCPDS # No. 49-1568). By contrast, as shown in Fig. 3g, the diffraction peaks of hollow and solid Fe/Mn/C nanocomplexes match well with $MnFeO_4$ crystal (JCPDS # No. 10-0319) and $Fe_{0.93}Mn_{0.04}N_{0.03}$ crystal (JCPDS # No. 47-1048). The special Fe-Co or Fe-Mn phase was well formed in the nanocomplex after pyrolysis in argon atmosphere.

For the carbon species in the nanocomplex, the Raman spectra in Figs 2h and 3h show two typical peaks at 1350 cm^{-1} (D band) and 1580 cm^{-1} (G band). As well known, D band is related to defect/disordered carbons and G band represents stretching vibration of sp^2 graphitic carbons, where the integral intensity ratio (I_D/I_G) can be applied to evaluate the graphitization degree of carbons [20]. The I_D/I_G for solid Fe/Co/C-800, solid Fe/Co/C-900, hollow Fe/Co/C-800 and hollow Fe/Co/C-900 (the number denotes pyrolytic temperature) were 1.24, 1.06, 1.42 and 1.15, respectively. Similarly, the I_D/I_G ratios for solid Fe/Mn/C-800, solid Fe/Mn/C-900, hollow Fe/Mn/C-800 and hollow Fe/Mn/C-900 were 0.87, 0.82, 1.09 and 0.98, respectively. The decreased I_D/I_G at higher temperature indicates the positive contribution for enhancing the graphitization degree of nanocomplex. Both hollow Fe/Co/C and hollow Fe/Mn/C show higher I_D/I_G than their solid analogues at the same pyrolysis temperature. Since high I_D/I_G means more defects or disorders that will lead to low electronic conductivity and high dielectric loss [48], the comprehensive effect of graphitization degree is very important for EM wave absorption as discussed later.

The PBAs and derived nanocomplexes with different topologies displayed typical type-IV isotherms with hysteresis loops in the relative pressure (P/P_0) range of 0.6–1.0 (Figs S3–S5). The BET specific surface area of the nanocomplexes gradually decreased as elevating pyrolytic temperature. The pore size was mainly below 32 nm (Table S1). During the transformation from PBAs to nanocomplexes, as shown in Figs 2 and 3, the decomposition of organic components and the collapse of cubic frameworks occurred at the same time at high temperatures. It also led to a rapid decrease in the specific surface area of the resultant nanocomplex. Anyway, the hollow topology and mesoporous structure are helpful to reduce the density and enhance the multi-RL of EM wave inside the nanocomplex.

Magnetic and dielectric properties of hollow and solid Fe/Co/C and Fe/Mn/C nanocomplexes

Considering that magnetic response is a crucial factor to EM wave absorption, the dependence of magnetic field on the magnetization of nanocomplexes is shown in Figs 2i and 3i. A significant hysteresis loop was observed. From the saturation magnetization (M_s), coercive force (O_e) and magnetic susceptibility ($\chi>0$) shown in Table S1, it can be concluded that all the Fe/Co/C nanocomplexes display ferromagnetic behavior due to the unsaturated 3d orbital electron interaction between the ferromagnetic metal iron and cobalt. On the contrary, the M_s, O_e and χ of Fe/Mn/C nanocomplexes are almost close to zero because the antiferromagnetic manganese neutralizes the ferromagnetic metallic iron in this case. Therefore, the EM wave attenuation in Fe/Mn/C nanocomplex can only be dependent on dielectric loss and multiple RL in hollow and mesoporous structure. Nevertheless, the magnetic response of either hollow or solid Fe/Co/C nanocomplexes is positive to EM wave absorption.

In general, complex permittivity ($\varepsilon_r=\varepsilon'-j\varepsilon''$) and permeability ($\mu_r=\mu'-j\mu''$) are often used as key EM parameters to evaluate the loss mechanism of absorbers [49]. The impedance ($\eta=\sqrt{\mu/\varepsilon}$) of EM absorption materials determines whether the incident EM wave is reflected or transmitted on the material surface. The EM parameters can be tuned by the phase composition and topology of the nanocomplexes. The ε' and ε'' in Fig. S6 decreased from ~20 to ~3 and from ~13 to ~1 for all the Fe/Co/C nanocomplexes, respectively. The ε' and ε'' of solid Fe/Co/C-900 were higher, indicating higher energy storage and dielectric loss of EM wave. The distinct peak bump of ε'' in 3–8 GHz for solid Fe/Co/C-800 indicated strong dielectric loss capacity. In contrast, the ε' and ε'' of solid nanocomplexes were both higher than hollow ones under the same pyrolysis temperature in most cases. For Fe/Mn/C nanocomplexes, the ε' ranging from ~16 to ~4 also exhibited dispersion behavior as the frequency increased (Fig. S7). However, the dependence of ε'' on frequency showed a relatively violent fluctuation. In the same way, the complex permittivity for solid Fe/Mn/C was higher than that for the hollow ones under the same pyrolytic conditions in most cases. The permittivity is related to the degree of graphitization and resultant electronic conductivity. As shown in Fig. 3, the enhanced permittivity is mainly due to some carbon nanorods existing in the solid Fe/Mn/C nanocomplex.

Fig. S8 illustrates the frequency dependence of complex permeability for ferromagnetic hollow and solid Fe/Co/C nanocomplexes derived at different pyrolytic temperatures. The μ' and μ'' of solid Fe/Co/C are higher than that of hollow Fe/Co/C in most cases. The initial susceptibility (χ>0) in Table S1 indicated ferromagnetic response behavior according to the following Equations (1–3) [50]:

$$\chi = M / H, \tag{1}$$

$$\mu' = 1 + (M / H)\cos\sigma, \tag{2}$$

$$\mu'' = 1 + (M / H)\sin\sigma, \tag{3}$$

where M is the magnetization, H the external magnetic field, and σ the phase lag angle of magnetization behind the external magnetic field.

For the Fe/Co/C nanocomplex, the complex permeability is distinctly different with frequency, where the μ' varies from 0.8 to 1.6 and the μ'' varies from 0 to 0.7, respectively. The solid Fe/Co/C-800 shows the highest μ' and μ'' among all the Fe/Co/C nanocomplexes. If the pyrolysis temperature rises to 900°C, which is close to the Curie temperature of metallic cobalt, the permeability will decrease. Compared with μ' and μ'', the saturation magnetization is less than 1 for all the Fe/Mn/C nanocomplexes. It should be pointed out that the permeability for some samples in 6–18 GHz increased as presented in Figs S8 and S9. Although it is abnormal due to the Snoek limit for traditional ferromagnetic materials, the microcurrent loop and EM induction induced by heterostructure anisotropy might be the main reason [51]. As illustrated in Figs 2f and 3f, the graphitic carbons or nanorods were distributed on or around the surface of cubic Fe/Mn or Fe/Co particles to form the heterostructure. Similar to expanded graphite/Fe_3O_4 nanoring composites [51], the conductive networks were formed with the graphitic carbons or nanorods and cubic Fe/Mn or Fe/Co particles in the nanocomplexes. The microcurrent loop could be formed around different interfaces of cubic magnetic nanoparticles, resulting in EM induction. It might be the main reason for the increase of permeability for either Fe/Co/C or Fe/Mn/C nanocomplexes. At the same time, the magnetic hysteresis loop almost coincides with the initial response curve. The initial susceptibility (χ = 0) in Table S1 indicates that the contribution of magnetic loss for EM wave absorption can be neglected. The dielectric loss will play a key role for Fe/Mn/C nanocomplexes.

EM wave absorption performance of hollow and solid Fe/Co/C and Fe/Mn/C nanocomplexes

The EM wave RLs of hollow and solid Fe/Co/C and Fe/Mn/C nanocomplexes were calculated based on the complex permittivity and permeability according to the transmission line theory using the following Equations (4) and (5) [52,53].

$$\mathrm{RL}=20\log_{10}\left|\frac{Z_{\mathrm{in}}-1}{Z_{\mathrm{in}}+1}\right|, \tag{4}$$

$$Z_{\mathrm{in}} = \sqrt{\frac{\mu_{\mathrm{r}}}{\varepsilon_{\mathrm{r}}}}\tanh\left[j\frac{2\pi fd}{c}\sqrt{\mu_{\mathrm{r}}\varepsilon_{\mathrm{r}}}\right], \tag{5}$$

where Z_{in}, μ_{r} and ε_{r} are the normalized input impedance, permittivity, and permeability, respectively. The f, d and c represent the microwave frequency, thickness of sample and the velocity of the EM wave in vacuum, respectively. In general, the RL value of less than −10 dB represents that EM wave is attenuated at least 90%.

In Fig. 4, the RLs *versus* frequency for all samples at the same thicknesses of 2.0 and 2.5 mm are presented. It can be seen that the EM wave attenuation is strongly dependent on the phase compositions and topologies of the nanocomplexes. Compared with Fe/C nanocomplex derived from PB under the same pyrolysis condition (Fig. S10), the minimum RL of solid Fe/Co/C-900 reaches −54.6 dB at 16.1 GHz with a thickness of 2.0 mm (Fig. 4). The attenuation ability of EM wave is greatly improved after the introduction of cobalt. Meanwhile, the EAB of solid Fe/Co/C-900 achieves 8.8 GHz at a thickness of 2.5 mm. The EAB and RL value show an obvious diversity with different thicknesses, pyrolysis temperatures and topological structures. The solid Fe/Co/C-800 possesses lower RL and higher EAB than hollow Fe/Co/C-800 at the same thickness. And the EAB of solid Fe/Co/C-900 is also higher than that of hollow Fe/Co/C-900 with a thickness of 2.5 mm (Fig. 4a, b). The difference in absorption is mainly caused by topological structure and the graphitization degree of carbon as depicted in Fig. 5a, b. Compared with hollow Fe/Co/C, the solid Fe/Co/C wrapped with carbon nanorods possesses higher I_D/I_G and degree of graphitization. The graphitization and carbon nanorods provide more efficient dielectric loss. Hence, the solid box-like Fe/Co/C shows strong EM wave absorption and broad bandwidth.

However, for the Fe/Mn/C nanocomplex, the EAB and RL for hollow Fe/Mn/C-800 are obviously better than those of solid Fe/Mn/C-800. As shown in Fig. 4c, the EAB of hollow Fe/Mn/C-800 is 6.7 GHz, higher than that of solid Fe/Mn/C-800 (4.7 GHz) at the same thickness of 2.5 mm. Similarly, the EAB of hollow Fe/Mn/C-900 (3.3 GHz) is also higher than that of solid Fe/Mn/C-900 (2.9 GHz) at the same thickness (Fig. 4d). The phenomenon is attributed to the hollow cage structure of

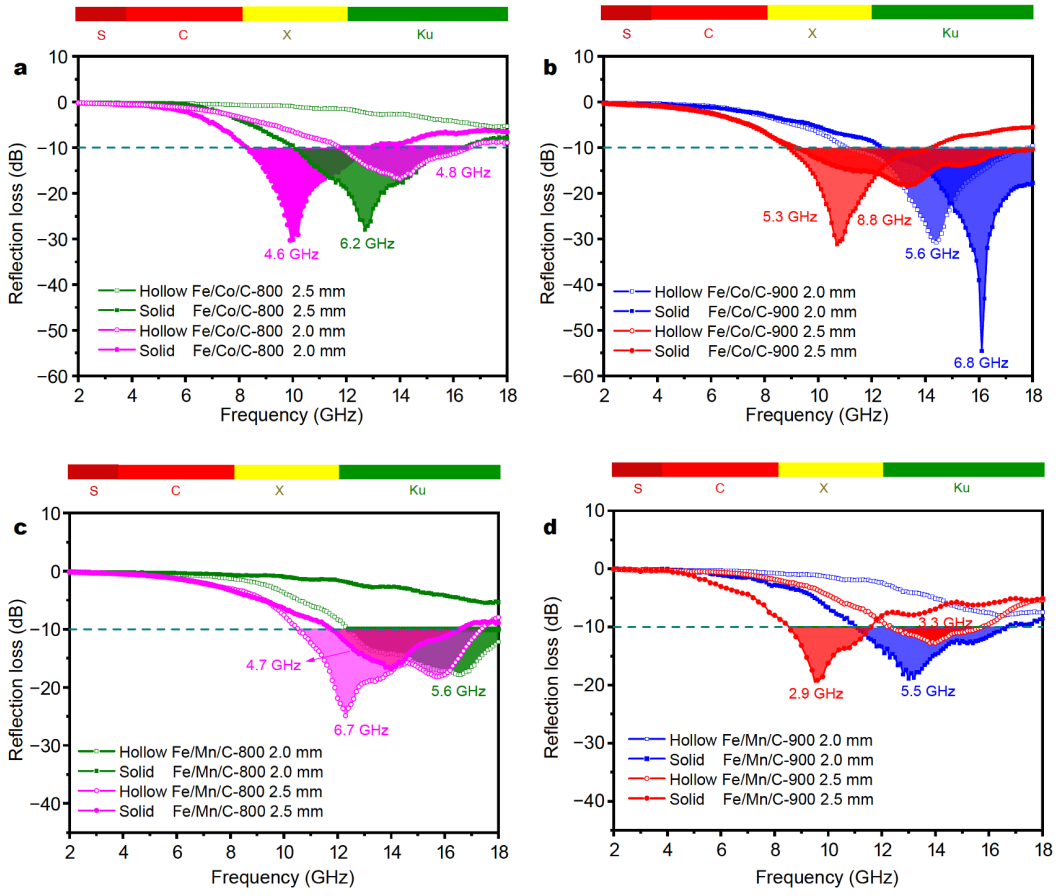

Figure 4 The comparison of EM wave absorption performance for pyrolyzed Fe/Co/C and Fe/Mn/C nanocomplexes. RL of (a) solid and hollow Fe/Co/C-800 nanocomplexes, (b) solid and hollow Fe/Co/C-900 nanocomplexes, (c) solid and hollow Fe/Mn/C-800 nanocomplexes and (d) solid and hollow Fe/Mn/C-900 nanocomplexes.

Fe/Mn/C nanocomplex. As shown in Fig. 5c, d, the EM wave enters the hollow structure and leads to the multiple RL and dielectric loss, enhancing the absorption performance, i.e., high EAB and low RL. On the contrary, it is difficult for EM wave to penetrate into the interior due to the higher value of permittivity and solid structure of solid Fe/Mn/C-900. In addition, the hollow Fe/Mn/C-800 has broader EAB and RL than solid Fe/Mn/C-800. It is confirmed that hollow structures with the suitable EM parameters can efficiently enhance the EM wave absorption.

The EM wave attenuation constant (α) in the interior of hollow cages and solid boxes can be accessed *via* the following Equation (6) [20,54]:

$$\alpha=\frac{\sqrt{2}\pi f}{c}\times\sqrt{(\mu''\varepsilon''-\mu'\varepsilon')+\sqrt{(\mu'\varepsilon''+\mu''\varepsilon')^2+(\mu''\varepsilon''-\mu'\eta')^2}}. \quad (6)$$

As shown in Fig. S11, an obvious increase of α in 8–18 GHz can be observed for all the nanocomplexes. The solid Fe/Co/C-900 exhibits the highest α, which is consistent with the maximum absorption and EAB with a thickness of 2.5 mm. Similarly, the hollow Fe/Mn/C-900 also has the maximum α, though it does not show the best absorption bandwidth and absorption intensity as illustrated in Fig. 4d. Of course, the highest α cannot fully prove that the nanocomplex has strong EM wave absorption ability. It also requires impedance characteristic of absorbers close to that of the free space calculated by Equation (1). The frequency dependence of $|Z_{in}/Z_0|$ for all samples is shown in Figs S12 and S13. The value of $|Z_{in}/Z_0|$ is close to 0.8–1.2, close to the best impedance matching. The value of $|Z_{in}/Z_0|$ for solid Fe/Co/C-900 is close to 0.9 when the EAB achieves maximum at a thickness of 2.5 mm. In this case, the incident EM wave can enter the absorber to a great extent as the optimal

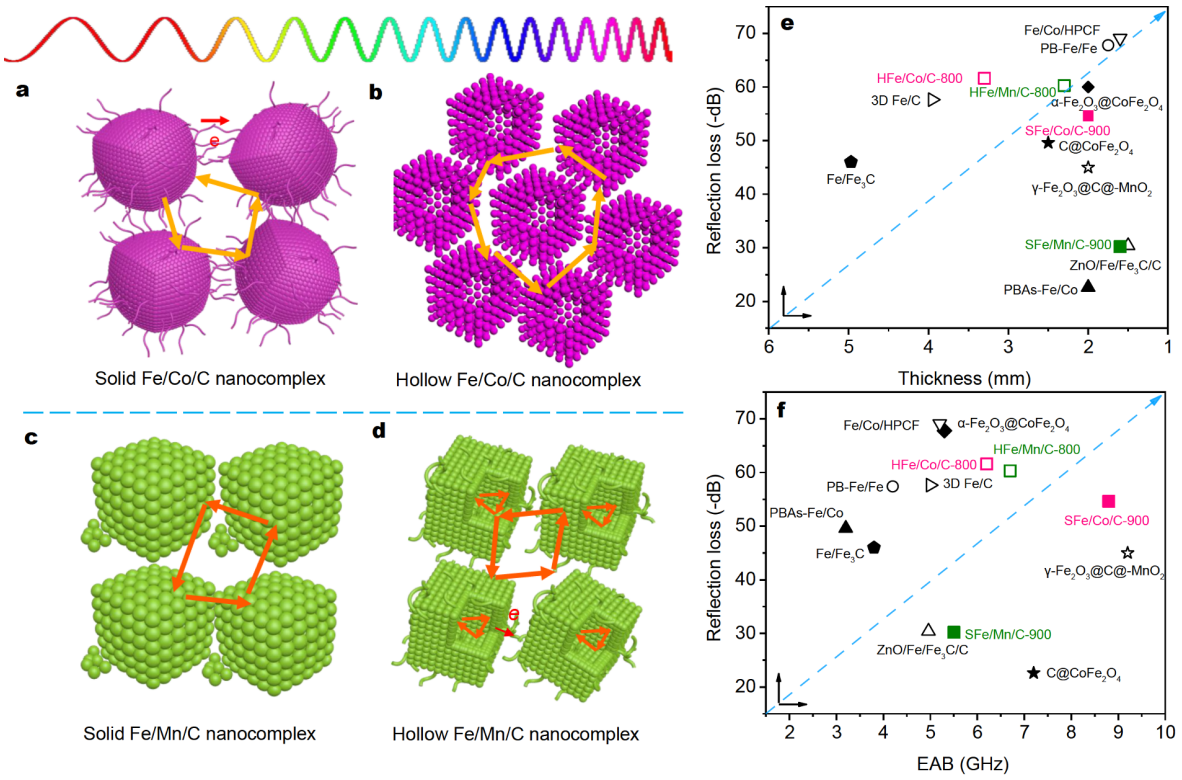

Figure 5 The proposed diagrams for multi RL and interfacial polarization mechanism of EM wave absorption. (a) Carbon network grown on the surface of solid Fe/Co/C nanocomplex, (b) the Fe/Co/C particles fall off from the surface and inside of the hollow Fe/Co/C nanocomplex, (c) the Fe/Mn/C particles fall off from the surface of solid Fe/Mn/C nanocomplex and (d) the carbon nanorods grown on or between hollow Fe/Mn/C nanocomplexes. The summary of EM wave absorption with (e) RL *vs*. thickness and (f) RL *vs*. EAB from different MOF-derived metal/carbon complexes.

impedance matching. However, the value of $|Z_{in}/Z_0|$ for solid Fe/Mn/C-800 is below 0.8, so its RL is above −10 dB in correspondence with the impedance mismatching feature at a thickness of 2.0 mm.

Compared with Fe-based hybrids or metal/carbon nanocomposites-derived MOFs reported previously, both Fe/Co/C and Fe/Mn/C nanocomplexes exhibited excellent EM wave absorption in the frequency range of 2–18 GHz. As illustrated in Fig. 5e, f and Table S2, the top right corner represents the optimal EM wave performance. The solid Fe/Co/C-900, hollow Fe/Co/C-800 and hollow Fe/Mn/C-800 all show favorable optimal EM wave absorbing abilities from the viewpoint of either EAB or RL. In details, for the Fe/Mn/C nanocomplex, the hollow Fe/Mn/C-800 shows the best EM wave absorption from the viewpoint of both RL and EAB. For Fe/Co/C nanocomplex, the solid Fe/ Co/C-900 possesses the best EM wave absorption. The EAB of 8.8 GHz at a thickness of 2.5 mm for solid Fe/Co/C-900 is a new record for this type of materials. As shown in Fig. 5a–d, in addition to reflection and transmission, the interface polarization is also important for absorbers. The graphitic carbons or nanorods in nanocomplexes provide more interfaces, enhancing the interface polarization. The migration of electric dipoles induced by interfacial polarization leads to dissipation of EM wave in absorbers. Therefore, a broad EAB was achieved in solid Fe/Co/C-900 nanocomplex.

For further analysis, the EM loss mechanisms of Fe/Co/C and Fe/Mn/C are different. For Fe/Co/C, the magnetic loss, dielectric loss and interface polarization, as well as the carbon nanorods-wrapped FeCo magnetic core are beneficial for enhancing the EM wave absorption. The interface polarization and magnetic loss induce high EM wave attenuation. That is the reason that solid Fe/Co/C possesses better absorption than hollow Fe/Co/C. On the contrary, the contribution of magnetic loss is almost zero as for Fe/Mn/C, and the dielectric loss and multi reflection in the hollow cage-like nanostructure become the main factor to EM wave attenuation. In the future design

of highly efficient EM wave absorbing materials using MOFs, the magnetic loss, dielectric loss, phase composition and topology should be considered in a comprehensive perspective.

CONCLUSIONS

The PBA hollow cages and solid boxes were synthesized through the coprecipitation method and the pyrolyzed hollow cage-like or solid box-like magnetic/dielectric Fe/Co/C and dielectric Fe/Mn/C nanocomplexes were obtained with controllable topological structures. The solid box-like Fe/Co/C-900 and hollow Fe/Mn/C all showed favorable absorbing abilities from the viewpoint of either EAB or RL. For solid box-like Fe/Co/C-900, the EAB of 8.8 GHz at a thickness of 2.5 mm is a new record for this type of materials. The tuning of EM wave absorbing ability *via* topology-controllable MOFs is very important for the design of absorbers. And the highly efficient and broad absorbing nanocomplexes possess great potential in antenna housings, radomes, aero-engines and stealth aircrafts.

Received 11 March 2020; accepted 5 April 2020; published online 12 June 2020

1 Li X, Wang L, You W, *et al.* Morphology-controlled synthesis and excellent microwave absorption performance of $ZnCo_2O_4$ nanostructures *via* a self-assembly process of flake units. Nanoscale, 2019, 11: 2694–2702
2 Lv H, Yang Z, Wang PL, *et al.* A voltage-boosting strategy enabling a low-frequency, flexible electromagnetic wave absorption device. Adv Mater, 2018, 30: 1706343
3 Cao MS, Cai YZ, He P, *et al.* 2D MXenes: Electromagnetic property for microwave absorption and electromagnetic interference shielding. Chem Eng J, 2019, 359: 1265–1302
4 Liang C, Qin W, Wang Z. Cobalt doping-induced strong electromagnetic wave absorption in SiC nanowires. J Alloys Compd, 2019, 781: 93–100
5 Liu L, He N, Wu T, *et al.* Co/C/Fe/C hierarchical flowers with strawberry-like surface as surface plasmon for enhanced permittivity, permeability, and microwave absorption properties. Chem Eng J, 2019, 355: 103–108
6 Chen KJ, Madden DG, Mukherjee S, *et al.* Synergistic sorbent separation for one-step ethylene purification from a four-component mixture. Science, 2019, 366: 241–246
7 Yang QY, Lama P, Sen S, *et al.* Reversible switching between highly porous and nonporous phases of an interpenetrated diamondoid coordination network that exhibits gate-opening at methane storage pressures. Angew Chem Int Ed, 2018, 57: 5684–5689
8 Chen KJ, Scott HS, Madden DG, *et al.* Benchmark C_2H_2/CO_2 and CO_2/C_2H_2 separation by two closely related hybrid ultramicroporous materials. Chem, 2016, 1: 753–765
9 Manna K, Zhang T, Carboni M, *et al.* Salicylaldimine-based metal-organic framework enabling highly active olefin hydrogenation with iron and cobalt catalysts. J Am Chem Soc, 2014, 136: 13182–13185
10 Zhang L, Wu HB, Madhavi S, *et al.* Formation of Fe_2O_3 microboxes with hierarchical shell structures from metal-organic frameworks and their lithium storage properties. J Am Chem Soc, 2012, 134: 17388–17391
11 He Z, Dai Y, Li X, *et al.* Hybrid nanomedicine fabricated from photosensitizer-terminated metal-organic framework nanoparticles for photodynamic therapy and hypoxia-activated cascade chemotherapy. Small, 2019, 15: 1804131
12 Begum S, Hassan Z, Bräse S, *et al.* Metal-organic framework-templated biomaterials: Recent progress in synthesis, functionalization, and applications. Acc Chem Res, 2019, 52: 1598–1610
13 Cao C, Ma D, Xu Q, *et al.* Semisacrificial template growth of self-supporting MOF nanocomposite electrode for efficient electrocatalytic water oxidation. Adv Funct Mater, 2019, 29: 1807418–1807426
14 Liu Y, Yang Y, Sun Y, *et al.* Ostwald ripening-mediated grafting of metal-organic frameworks on a single colloidal nanocrystal to form uniform and controllable MXF. J Am Chem Soc, 2019, 141: 7407–7413
15 Lü Y, Wang Y, Li H, *et al.* MOF-derived porous Co/C nanocomposites with excellent electromagnetic wave absorption properties. ACS Appl Mater Interfaces, 2015, 7: 13604–13611
16 Zhang K, Wu F, Xie A, *et al. In situ* stringing of metal organic frameworks by SiC nanowires for high-performance electromagnetic radiation elimination. ACS Appl Mater Interfaces, 2017, 9: 33041–33048
17 Liao Q, He M, Zhou Y, *et al.* Highly cuboid-shaped hetero-bimetallic metal-organic frameworks derived from porous Co/ZnO/C microrods with improved electromagnetic wave absorption capabilities. ACS Appl Mater Interfaces, 2018, 10: 29136–29144
18 Feng W, Wang Y, Chen J, *et al.* Metal organic framework-derived CoZn alloy/N-doped porous carbon nanocomposites: Tunable surface area and electromagnetic wave absorption properties. J Mater Chem C, 2018, 6: 10–18
19 Liao Q, He M, Zhou Y, *et al.* Rational construction of $Ti_3C_2T_x$/Co-MOF-Derived Laminated Co/TiO_2-C hybrids for enhanced electromagnetic wave absorption. Langmuir, 2018, 34: 15854–15863
20 Miao P, Cheng K, Li H, *et al.* Poly(dimethylsilylene)diacetylene-guided ZIF-based heterostructures for full Ku-band electromagnetic wave absorption. ACS Appl Mater Interfaces, 2019, 11: 17706–17713
21 Yin Y, Liu X, Wei X, *et al.* Porous CNTs/Co composite derived from zeolitic imidazolate framework: A lightweight, ultrathin, and highly efficient electromagnetic wave absorber. ACS Appl Mater Interfaces, 2016, 8: 34686–34698
22 Yin Y, Liu X, Wei X, *et al.* Magnetically aligned Co-C/MWCNTs composite derived from MWCNT-Interconnected zeolitic imidazolate frameworks for a lightweight and highly efficient electromagnetic wave absorber. ACS Appl Mater Interfaces, 2017, 9: 30850–30861
23 Shu R, Li W, Wu Y, *et al.* Nitrogen-doped Co-C/MWCNTs nanocomposites derived from bimetallic metal-organic frameworks for electromagnetic wave absorption in the X-band. Chem Eng J, 2019, 362: 513–524
24 Zhou C, Wu C, Liu D, *et al.* Metal-organic framework derived hierarchical Co/C@V_2O_3 hollow spheres as a thin, lightweight, and high-efficiency electromagnetic wave absorber. Chem Eur J, 2019, 25: 2234–2241
25 Yang Z, Lv H, Wu R. Rational construction of graphene oxide with MOF-derived porous NiFe@C nanocubes for high-performance

microwave attenuation. Nano Res, 2016, 9: 3671–3682
26 Zhang Y, Zhang HB, Wu X, *et al.* Nanolayered cobalt@carbon hybrids derived from metal-organic frameworks for microwave absorption. ACS Appl Nano Mater, 2019, 2: 2325–2335
27 Wang K, Chen Y, Tian R, *et al.* Porous Co-C core-shell nanocomposites derived from Co-MOF-74 with enhanced electromagnetic wave absorption performance. ACS Appl Mater Interfaces, 2018, 10: 11333–11342
28 Wu N, Xu D, Wang Z, *et al.* Achieving superior electromagnetic wave absorbers through the novel metal-organic frameworks derived magnetic porous carbon nanorods. Carbon, 2019, 145: 433–444
29 Xiang Z, Song Y, Xiong J, *et al.* Enhanced electromagnetic wave absorption of nanoporous Fe_3O_4@carbon composites derived from metal-organic frameworks. Carbon, 2019, 142: 20–31
30 Zhu BY, Miao P, Kong J, *et al.* Co/C composite derived from a newly constructed metal-organic framework for effective microwave absorption. Cryst Growth Des, 2019, 19: 1518–1524
31 Liu W, Liu L, Ji G, *et al.* Composition design and structural characterization of MOF-derived composites with controllable electromagnetic properties. ACS Sustain Chem Eng, 2017, 5: 7961–7971
32 Nai J, Lou XWD. Hollow structures based on Prussian blue and its analogs for electrochemical energy storage and conversion. Adv Mater, 2019, 31: 1706825
33 Deng L, Yang Z, Tan L, *et al.* Investigation of the Prussian blue analog $Co_3[Co(CN)_6]_2$ as an anode material for nonaqueous potassium-ion batteries. Adv Mater, 2018, 30: 1802510
34 Keggin JF, Miles FD. Structures and formulæ of the Prussian blues and related compounds. Nature, 1936, 137: 577–578
35 Nai J, Lu Y, Yu L, *et al.* Formation of Ni-Fe mixed diselenide nanocages as a superior oxygen evolution electrocatalyst. Adv Mater, 2017, 29: 1703870
36 Li Y, Hu J, Yang K, *et al.* Synthetic control of Prussian blue derived nano-materials for energy storage and conversion application. Mater Today Energy, 2019, 14: 100332
37 Du Y, Chen J, Li L, *et al.* Core-shell FeCo Prussian blue analogue/$Ni(OH)_2$ derived porous ternary transition metal phosphides connected by graphene for effectively electrocatalytic water splitting. ACS Sustain Chem Eng, 2019, 7: 13523–13531
38 Miao P, Zhou R, Chen K, *et al.* Tunable electromagnetic wave absorption of supramolecular isomer-derived nanocomposites with different morphology. Adv Mater Interfaces, 2020, 7: 1901820
39 Qiang R, Du Y, Zhao H, *et al.* Metal organic framework-derived Fe/C nanocubes toward efficient microwave absorption. J Mater Chem A, 2015, 3: 13426–13434
40 Liu D, Qiang R, Du Y, *et al.* Prussian blue analogues derived magnetic FeCo alloy/carbon composites with tunable chemical composition and enhanced microwave absorption. J Colloid Interface Sci, 2018, 514: 10–20
41 Panwar R, Puthucheri S, Singh D. Experimental demonstration of novel hybrid microwave absorbing coatings using particle-size-controlled hard-soft ferrite. IEEE Trans Magn, 2018, 54: 1–5
42 Zhou M, Zhang X, Wei J, *et al.* Morphology-controlled synthesis and novel microwave absorption properties of hollow urchinlike α-MnO_2 nanostructures. J Phys Chem C, 2011, 115: 1398–1402
43 Zhao B, Zhao W, Shao G, *et al.* Morphology-control synthesis of a core-shell structured NiCu alloy with tunable electromagnetic-wave absorption capabilities. ACS Appl Mater Interfaces, 2015, 7: 12951–12960
44 Nai J, Zhang J, Lou XWD. Construction of single-crystalline Prussian blue analog hollow nanostructures with tailorable topologies. Chem, 2018, 4: 1967–1982
45 Zheng F, Zhu D, Shi X, *et al.* Metal-organic framework-derived porous $Mn_{1.8}Fe_{1.2}O_4$ nanocubes with an interconnected channel structure as high-performance anodes for lithium ion batteries. J Mater Chem A, 2015, 3: 2815–2824
46 Cai X, Gao W, Ma M, *et al.* A Prussian blue-based core-shell hollow-structured mesoporous nanoparticle as a smart theranostic agent with ultrahigh pH-responsive longitudinal relaxivity. Adv Mater, 2015, 27: 6382–6389
47 Zakaria MB, Hu M, Hayashi N, *et al.* Thermal conversion of hollow Prussian blue nanoparticles into nanoporous iron oxides with crystallized hematite phase. Eur J Inorg Chem, 2014, 2014: 1137–1141
48 Zhu T, Chang S, Song YF, *et al.* PVP-encapsulated $CoFe_2O_4$/rGO composites with controllable electromagnetic wave absorption performance. Chem Eng J, 2019, 373: 755–766
49 Song Y, He L, Zhang X, *et al.* Highly efficient electromagnetic wave absorbing metal-free and carbon-rich ceramics derived from hyperbranched polycarbosilazanes. J Phys Chem C, 2017, 121: 24774–24785
50 Liu S, Liu J, Dong X. Electromagnetic Shielding and Absorbing Materials. 2nd ed. Beijing: Chemical Industry Press, 2014, 418
51 Zhao Y, Liu L, Jiang K, *et al.* Distinctly enhanced permeability and excellent microwave absorption of expanded graphite/Fe_3O_4 nanoring composites. RSC Adv, 2017, 7: 11561–11567
52 Luo C, Jiao T, Gu J, *et al.* Graphene shield by SiBCN ceramic: A promising high-temperature electromagnetic wave-absorbing material with oxidation resistance. ACS Appl Mater Interfaces, 2018, 10: 39307–39318
53 Luo C, Tang Y, Jiao T, *et al.* High-temperature stable and metal-free electromagnetic wave-absorbing SiBCN ceramics derived from carbon-rich hyperbranched polyborosilazanes. ACS Appl Mater Interfaces, 2018, 10: 28051–28061
54 Li J, Miao P, Chen KJ, *et al.* Highly effective electromagnetic wave absorbing prismatic Co/C nanocomposites derived from cubic metal-organic framework. Compos Part B-Eng, 2020, 182: 107613

Acknowledgements This work was financially supported by the National Natural Science Foundation of China (21875190), Polymer Electromagnetic Functional Materials Innovation Team of Shaanxi Sanqin Scholars, the Natural Science Basic Research Plan in Shaanxi Province of Distinguished Young Scholar (2018JC-008), and China Postdoctoral Science Foundation (2018M643724).

Author contributions Kong J and Chen KJ designed the experiments. Kong J led the project. Miao P and Chen J conducted and performed the experiments. Kong J, Chen KJ and Tang Y analyzed the data. Miao P, Kong J and Chen KJ wrote the manuscript. All authors contributed to the general discussion.

Conflict of interest The authors declare that they have no conflict of interest.

Supplementary information Supporting data are available in the online version of the paper.

Peng Miao received his master degree in materials physics and chemistry from Chang'an University in 2014. He is currently a PhD candidate majored in chemistry under the supervision of Prof. Jie Kong at Northwestern Polytechnical University. His research interest mainly focuses on the synthesis of metal-organic frameworks and their applications in electromagnetic absorption and shielding.

Jie Kong received his PhD degree from Northwestern Polytechnical University in 2004. He then went to The Hong Kong Polytechnic University as a postdoctoral fellow and the University of Bayreuth as an Alexander von Humboldt research fellow. In 2011, he joined the School of Science at Northwestern Polytechnical University as a full professor. His research interests include hyperbranched polymers, metal-organic frameworks, ceramic precursors and electromagnetic absorbing/transmitting materials.

金属有机框架衍生高效宽频电磁波吸收剂拓扑结构调控研究

苗鹏, 陈建新, 唐玉生, 陈凯杰, 孔杰*

摘要 装备隐身和电子器件电磁防护的发展对高带宽、强吸收先进电磁波吸收材料具有迫切需求, 采用金属有机骨架(MOF)衍生有序结构金属/碳杂化材料是重要制备方法. 本文采用具有可控拓扑结构和微相组成的普鲁士蓝衍生物作为前驱体, 通过热解工艺制备空心、实心的笼状、盒状等拓扑结构Fe/Co/C和Fe/Mn/C纳米复合电磁波吸收剂. 实心Fe/Co/C和空心Fe/Mn/C均表现出强电磁吸收和高吸收带宽, 电磁波反射系数最低为−54.6 dB, 其中900°C热解制备的实心盒状Fe/Co/C吸收剂在厚度2.5 mm时有效吸收带宽高达8.8 GHz, 刷新了该类材料的性能上限. 通过控制MOF拓扑结构来设计和调控金属/碳杂化吸波剂对于新型电磁波吸收材料的发展及其在装备隐身领域的应用具有重要意义.

